

1 **Impacts of hemispheric solar geoengineering on tropical** 2 **cyclone frequency**

3 Anthony C. Jones^{1,2}*, James M. Haywood^{1,2}, Nick Dunstone², Kerry Emanuel³, Matthew K.
4 Hawcroft¹, Kevin I. Hodges⁴, and Andy Jones²

5 [1]{College of Engineering Maths and Physical Sciences, University of Exeter, Laver
6 Building, North Park Road, Exeter, UK, EX4 4QE}

7 [2]{Met Office Hadley Centre, Fitzroy Road, Exeter, UK, EX1 3PB}

8 [3]{Center for Global Change Science, Massachusetts Institute of Technology, 77
9 Massachusetts Avenue, Cambridge, USA, MA 02139}

10 [4]{Department of Meteorology, University of Reading, PO Box 243, Earley Gate,
11 Reading RG6 6BB}

12 Correspondence to: Anthony C. Jones (anthony.jones@metoffice.gov.uk)

13 **Abstract**

14 Solar geoengineering refers to a range of proposed methods for counteracting global warming
15 by artificially reducing sunlight at Earth's surface. The most widely known solar
16 geoengineering proposal is stratospheric aerosol injection (SAI) which has impacts analogous
17 to those from volcanic eruptions. Observations following major volcanic eruptions indicate
18 that aerosol enhancements confined to a single hemisphere effectively modulate North
19 Atlantic tropical cyclone (TC) activity in the following years. Here we investigate the effects
20 of both single-hemisphere and global SAI scenarios on North Atlantic TC activity using the
21 HadGEM2-ES general circulation model and various TC identification methods. We show
22 that a robust result from all of the methods is that SAI applied to the southern hemisphere
23 would enhance TC frequency relative to a global SAI application, and vice versa for SAI in
24 the northern hemisphere. Our results reemphasize concerns regarding regional
25 geoengineering and should motivate policymakers to regulate large-scale unilateral
26 geoengineering deployments.

27 **Main text**

28 **Introduction**

29 In the last decade, solar geoengineering (SG) has rapidly garnered attention as a plausible
30 method to counteract global warming [1,2,3]. Studies with general circulation models
31 (GCMs) indicate that SG could effectively cool the Earth's surface, at the expense of regional
32 climate changes [4], but these regional changes would be less severe than those in a non-
33 geoengineered world [5]. A study has been performed (Ref. 6) on the frequency and intensity
34 of Atlantic hurricanes and associated storm surges using a multi-model analysis of
35 Geoengineering Model Intercomparison Project (GeoMIP) scenarios G3 and G4 [7], where
36 stratospheric aerosol injection (SAI) is applied relatively uniformly to both hemispheres.
37 However, a growing number of studies have investigated regional SG application scenarios,
38 which could prove preferential to a global application by restricting the geospatial magnitude
39 of the climate response or by being used to target specific climate changes [8,9,10,11]. SAI
40 does not easily lend itself to regional impositions due to the rapid dispersion of aerosols in the
41 stratosphere. Nevertheless, SAI could be contained or promoted in a single hemisphere due to
42 the general poleward transport tendency of the stratospheric circulation [8,11]. Preferential
43 aerosol injection in a single hemisphere would alter tropical sea-surface temperature (SST)
44 gradients and displace the Inter-Tropical Convergence Zone (ITCZ) toward the opposite
45 hemisphere as observed following the 20th century Katmai (1912) and El Chichón (1982)
46 volcanic eruptions [11,12]. Consequentially, SAI concentrated in the northern hemisphere
47 (NH) would likely reduce rainfall over the Sahel and vice versa for SAI in the southern
48 hemisphere (SH) [11].

49 Another phenomenon related to the location of the ITCZ is North Atlantic tropical cyclone
50 (TC) frequency [13,14]. An ITCZ displaced to the north provides optimal conditions for
51 cyclogenesis promotion from African easterly waves (AEWs) in the hurricane main
52 development region (MDR, defined as [5°-20°N, 15°-85°W]), which results in anomalously
53 high TC activity [13,14,15]. In contrast, an ITCZ displaced to the south is associated with
54 increased wind-shear over the MDR and attenuated TC activity. TC activity was significantly
55 attenuated followed the El Chichón (1982) and Pinatubo (1991) volcanic eruptions, both of
56 which primarily enhanced the NH aerosol burden [16,17]. Conversely, the Tambora (1815)
57 and Agung (1963) volcanic eruptions primarily enhanced the SH aerosol burden, and were
58 subsequently followed by periods of enhanced TC activity [17]. Additionally, GCM studies
59 have implicated periods of high (low) NH-centric anthropogenic aerosol emissions with

60 attenuated (enhanced) TC activity in the 20th Century (Supplementary Note 1) [13], which
61 further corroborates the relationship between asymmetric aerosol burdens and TC activity. As
62 regional SAI applications have been proposed to specifically target, for instance, NH sea-ice
63 concentrations [8] and would necessarily alter the inter-hemispheric aerosol gradient, it is
64 instructive to assess the implications of global and regional SAI scenarios on North Atlantic
65 TC activity.

66 In this study we investigate North Atlantic TCs in simulations performed using the
67 HadGEM2-ES GCM in a fully-coupled atmosphere-ocean configuration [18] by directly
68 tracking TC-like features [19], by utilising various metrics that have been developed as
69 proxies for TC activity [13,20,21], and by employing a widely-used statistical-dynamical
70 downscaling model [22] (see Methods). Our motivation for using different TC-identification
71 methods is the significant disparity in projections of future TC activity in the North Atlantic
72 basin between studies with alternative algorithms [21,23,24]. In particular, the results of
73 GCM studies mostly agree that overall TC frequency decreases under global warming, but
74 that the frequency of the most intense storms increases [19,23,25]. Conversely, the results of
75 applying statistical-dynamical downscaling to CMIP5 output suggest a steady increase in
76 North Atlantic TC frequency under global warming [24]. In contrast, the results of applying a
77 statistical relationship between TC activity and relative SSTs to CMIP5 output showed no
78 robust trend in TC activity changes under global warming [21]. We have therefore decided to
79 utilize all 3 different approaches (explicit storms, statistical relationships, and downscaling)
80 for comparison purposes and due to their relative merits (Supplementary Note 2). Note that
81 on top of these TC identification methods, other methods have also been developed such as
82 ‘dynamical downscaling’ which involves embedding a high-resolution climate model within
83 a GCM [26], and alternative explicit TC identification algorithms such as the Camargo-
84 Zebiak algorithm [27].

85 We assess 2 ensemble members for the recent historical period (1950-2005, hereafter denoted
86 HIST) and 3 ensemble members for the Representative Concentration Pathway (RCP) 4.5
87 scenario (2006-2089). For SAI, we assess 3 ensemble members for a global SAI scenario (G4
88 [7]) in which a constant injection rate of 5 Tg of sulfur dioxide (SO₂) per year is applied
89 uniformly over the globe from 2020-2070, and 1 simulation each for NH-only (G4NH) and
90 SH-only (G4SH) SAI scenarios in which 5 Tg[SO₂] y⁻¹ is injected evenly over the
91 hemisphere from 2020-2070 [11]. We assess the impact of SAI cessation by abruptly
92 suspending aerosol injection in year 2070 in G4/G4NH/G4SH and allowing the model to run

93 for a further 20 years. To analyse TC frequency, we utilise ERA-interim (ERA-I) reanalyses
94 for the period 1979-2014 [28] and compare the ERA-I and simulated TC frequency with
95 observations from the HURDAT2 Best Tracks dataset [29]. We employ a widely-used feature
96 tracking software (TRACK) [19] to track vorticity maxima over the North Atlantic basin in
97 the simulations and reanalysis data. The additional TC proxy metrics that are analysed are
98 June-November (JJASON) precipitation in the MDR, vertical zonal-wind shear between 850
99 hPa and 250 hPa in the MDR ($U_{850}-U_{250}$), and the difference between the SST in the MDR
100 and the tropics as a whole (denoted relative SST) [13]. We also utilise a statistical-dynamical
101 downscaling model to investigate changes to TC frequency and intensity [22,24]. For each of
102 these methods we find that TC activity is enhanced by SH-only SAI relative to a global SAI
103 application, and vice versa for NH-only SAI. We conclude that asymmetries in the climatic
104 response to hemispheric solar geoengineering should motivate policymakers to regulate
105 geoengineering so as to deter unilateral deployments.

106 **Results**

107 **Aerosol distribution.** It is important to assess whether single-hemisphere SAI scenarios are
108 feasible. The injection of aerosol into the stratosphere following a volcanic eruption can lead
109 to radically different spatial and temporal distributions depending upon the altitude and
110 latitude of the injection [30], the representation of the quasi-biennial oscillation (QBO; [31]),
111 and the local meteorological conditions that prevail at the time of the eruption [32]. We
112 demonstrate the sensitivity to altitude and latitude by performing volcanic eruption
113 simulations using an atmosphere only version of the HadGEM2-CCS model [32] with the
114 model top at approximately 84 km. The same amount of SO_2 was emitted at various different
115 altitudes and latitudes in the NH (the results from simulations emitting into the SH reveal a
116 strong similarity and are not shown here). It is immediately evident from Fig. 1 that only
117 injection strategies where SO_2 is injected into high altitudes (23-28 km) at equatorial latitudes
118 (Equator and $15^\circ N$) lead to an aerosol distribution that is approximately hemispherically
119 symmetric. Emissions at high altitudes (23-28 km) northward of $15^\circ N$ lead to aerosol
120 distributions that are significantly larger in the NH than the SH. Emissions at intermediate
121 altitudes of 16-23 km altitude result in aerosol predominantly in the NH. Emissions at low
122 altitude (11-15 km) are mostly below the tropopause leading to a much more limited lifetime
123 of the resultant aerosol, Given current technical challenges of any deliberate SAI scheme [33]
124 it is feasible that a sub-optimal SAI strategy (i.e. at mid-latitudes and/or at lower altitudes)
125 might conceivably be pursued.

126 We now consider the simulations in this study performed with the low-top version of the
127 HadGEM2 model. As in other studies [11,31,34,35,36] we compensate for the lack of
128 adequately resolved QBO owing to the limited height of the top of the model by injecting
129 over a wide range of latitudes rather than injecting at a single point. Figure 2 shows the
130 annual-mean sulfate (SO_4) aerosol optical depth (AOD) anomalies in the G4, G4NH and
131 G4SH simulations averaged over 2020-2070. It is clear that the SO_4 aerosol is primarily
132 confined to the hemisphere(s) of injection in all of the SAI scenarios.

133 **Climate changes.** Regional and global SAI applications would do much to ameliorate
134 changes in near-surface air temperature and sea-ice evident in the RCP4.5 scenario, with the
135 principal counteractive effect occurring in the hemisphere(s) of injection (Fig. 3). However,
136 the impacts in the un-geoengineered hemisphere would also be significant owing to
137 atmospheric and oceanic inter-hemispheric energy transport, for instance, in these simulations
138 an NH cooling of 0.7 K is observed in G4SH relative to RCP4.5 (2020-2070), compared to 1
139 K in G4 and 1.1 K in G4NH (Fig. 3b). This result corroborates previous research suggesting
140 that the impacts of SG would not be entirely confined to the perturbed region [4,8,10,11,12].

141 **Simulated Tropical Cyclones.** In the historical period, the model skilfully captures observed
142 TC frequency trends as inferred from TRACK ($r = 0.71$ with HURDAT) including the
143 decline in activity through 1960 to 1980 and the increase in activity since 1980 (Fig. 4a). The
144 annual-mean TC frequency in HIST is 10.4 (90% confidence intervals (CI): 5, 16) TCs y^{-1} ,
145 where the square brackets denote the 5-95% range. In RCP4.5, TC frequency decreases
146 between 2020 and 2070 (-0.3 TCs dec^{-1}) with an annual-mean frequency of 9.7 (90% CI: 4,
147 15) TCs y^{-1} , while in G4 TC frequency increases slightly relative to HIST (annual-mean =
148 11.2 (90% CI: 5, 18) TCs y^{-1}). The TC frequency changes between 2020-2070 and HIST in
149 the RCP4.5 and G4 scenarios are not statistically significant at the 5 % level (Supplementary
150 Note 3). G4SH exhibits a marked increase in TC frequency relative to HIST (annual-mean
151 TCs $\text{y}^{-1} = 14.3$ (90% CI: 8, 20)), while G4NH conversely exhibits a pronounced reduction
152 (annual-mean TCs $\text{y}^{-1} = 7.6$ (90% CI: 2, 13)). The G4NH and G4SH results are consistent
153 with observed TC activity changes following volcanic aerosol enhancements confined to a
154 single hemisphere [16,17]. TC frequency swiftly rebounds to concurrent RCP4.5 levels
155 following the cessation of SAI in G4, G4NH and G4SH in year 2070 (Fig. 4b), which
156 confirms that the solar geoengineering termination effect [37] extends to North Atlantic TC
157 activity. The TC frequency changes between 2020-2070 and HIST in the G4NH and G4SH
158 scenarios are statistically significant at the 5 % level (Supplementary Note 3).

159 **Tropical Cyclone proxies.** The progression of AEWs to TCs is contingent on the ambient
160 meteorological conditions, which may act to induce or dissipate the storm. For instance,
161 enhanced wind-shear over the MDR counteracts cyclogenesis [20], whereas a warm ocean
162 surface provides the storm vortex with energy [21]. Historical trends in MDR wind-shear,
163 precipitation and relative SST closely correlate with North Atlantic TC activity (Fig 1. in Ref.
164 13) and these indices offer an alternative tool to counting vortices for predicting future TC
165 trends. Figure 5 shows various North Atlantic TC indices as extracted from the HadGEM2-
166 ES simulations. It is clear that active (1950-1965, 1995-2014) and inactive (1965-1995) TC
167 periods in the HIST simulation (Fig. 4a) were commensurate with active and inactive periods
168 in the indices (Fig. 5). The same correlations between indices and TC frequency persist in the
169 RCP4.5 and SAI simulations, with G4SH and G4NH exhibiting continuously positive and
170 negative indices respectively (Fig. 5). This suggests that meteorological conditions presently
171 conducive to cyclogenesis remain conducive in these scenarios. Figure 6 shows maps of
172 precipitation, wind-shear and relative SST anomalies in the G4NH and G4SH scenarios. In
173 G4NH, aerosol-induced cooling of the North Atlantic sea-surface ($>30^{\circ}\text{N}$) results in a
174 southward shift and strengthening of the African easterly jet (AEJ), enhanced wind-shear in
175 the MDR, and anomalous descent and precipitation reduction over the MDR (Fig. 6a-c) [13].
176 Conversely, preferential cooling of the South Atlantic in G4SH enhances ascent and
177 precipitation in the MDR and shifts the AEJ north, reducing wind-shear over the MDR and
178 producing favourable conditions for cyclogenesis (Fig. 6d-f).

179 Figures 5 and 6 suggest that enhanced TC activity is related to certain climatic conditions in
180 the MDR, in particular enhanced precipitation, attenuated vertical wind-shear, and a warmer
181 sea surface (relative to the tropical mean). It is important to investigate these relationships
182 using observations and reanalyses to ascertain their practical robustness. Figure 7 shows time
183 series for TC frequency [29], precipitation and vertical wind-shear ($U_{850}-U_{25}$) [38], and
184 relative SSTs [39] from reanalyses and observations. From comparing Fig. 7a with Figs
185 7b,c,d, it appears that periods of enhanced TC activity in the 20th century coincided with
186 enhanced precipitation and relative SSTs and attenuated vertical wind-shear [13] which
187 substantiates our modelling results (Fig. 5). The closest relationship in terms of active and
188 inactive periods in Fig. 7 is between TC activity and relative SST. Statistical models for
189 count data using a Poisson distribution framework can be developed to quantify the observed
190 relationships between TC activity and MDR meteorology (Supplementary Note 4) [21].
191 Figure 8 shows time-series of TC activity from the HadGEM2-ES simulations as determined

192 by applying the statistical relationships from the historical observations (Fig. 7) to the
193 simulated meteorology, where the covariates are anomalies from the 1900-2005 mean values.
194 The covariate trends suggest enhanced (attenuated) TC activity in the G4SH (G4NH)
195 simulation between 2020-2070 relative to HIST and RCP4.5 (Fig. 8), which substantiates the
196 results of the explicit storm tracking (Fig. 4). We find little evidence to support the
197 hypothesis that the simulated TC frequency changes (Fig. 4) are the result of an El Niño
198 Southern Oscillation (ENSO) response, which further supports the ITCZ-TC connection
199 theory (Supplementary Note 5).

200 **Statistical-dynamical downscaling.** Statistical-dynamical downscaling models are able to
201 simulate the observed intensity distribution of North Atlantic TCs [40], whereas explicitly
202 simulated storms are not as intense as those observed (Supplementary Note 6). Therefore we
203 employ a downscaling model to investigate changes to the most intense storms under global
204 warming and SAI. Forced by HadGEM2-ES meteorology, the model is clearly able to
205 reproduce TC trends in the recent historical period (Fig. 9a), although the frequency of major
206 hurricanes (max windspeed $> 96 \text{ m s}^{-1}$) is undersimulated in the 1960s compared to
207 HURDAT observations (Fig. 9c). In contrast to the results of the explicit storms (Fig. 4), the
208 model shows a steadily increasing trend in TC frequency in the RCP4.5 scenario over 2020-
209 2070 (Fig. 9a), in agreement with the results of applying downscaling to the CMIP5 ensemble
210 using the RCP8.5 scenario [24]. SAI generally counteracts the intensification of TC activity
211 relative from RCP4.5, except in the interesting case of the first ~ 10 years in G4SH, which
212 exhibits an increase in major hurricane, hurricane and TC activity (Fig. 9c). G4SH
213 consistently produces the most TCs per year relative to the other SAI scenarios, with 2020-
214 2070 mean frequencies of 12.6, 8.8, and 3.3 TCs, hurricanes and major hurricanes per year
215 respectively. This can be compared to 10.5, 7.3, and 2.6 for G4NH; 10.8, 7.2, and 2.5 for G4;
216 and 15.3, 11.1, and 4.3 for RCP4.5. The TC frequencies in the SAI simulations are
217 significantly different to RCP4.5, and the G4SH TC frequencies are significantly greater than
218 G4 and G4NH (Supplementary Note 7). Following the cessation of SAI in 2070, TC activity
219 rebounds to the baseline RCP4.5 activity within ~ 15 years (Fig. 9a), again confirming that the
220 SG termination effect extends to North Atlantic TCs [31].

221 1. Discussion

222 A previous multi-model ensemble of GeoMIP G3 and G4 simulations [6] using a temperature
223 based proxy [41] found that geoengineering reduced hurricane frequency although the

224 statistical significance was marginal. Our results for hemispherically symmetric SAI (G4) are
225 similarly marginal using both the TC tracking algorithm and three different types of TC
226 proxy (Figs 4 and 8). However, when employing a statistical-dynamical downscaling
227 algorithm, we find that a global SAI application could reduce TC frequency significantly
228 relative to RCP4.5 (Fig. 9). This disparity between the results of explicit storm modelling
229 from GCM simulations and statistical-dynamical downscaling is not a new result and remains
230 fundamentally unexplained [23,24,42,43]. Nevertheless, there are important commonalities
231 between the results of the explicit storm modelling and statistical-dynamical downscaling.
232 The first is that SAI applied to the southern hemisphere would increase North Atlantic TC
233 activity relative to a global SAI application (Figs 4 and 9). The second commonality is that
234 the cessation of SAI would rapidly lead to TC activity rebounding to the base state climate.

235 The primary result of this research is to demonstrate that single-hemisphere SAI could
236 modulate North Atlantic TC frequency. However, a scenario in which TC frequency is
237 suppressed by NH SAI would unavoidably induce droughts in the Sahel, and vice versa for
238 SH SAI [11,44]. Ideally, our simulations would be replicated by a multi-model ensemble
239 [45]. Because the G4NH and G4SH simulations are unofficial variants of the G4 simulations
240 they have not been performed by other modelling centres. However, our results are likely to
241 be generally applicable owing to the large body of evidence that if a climate model is forced
242 by cooling one hemisphere, the ITCZ and associated precipitation will migrate towards the
243 opposite hemisphere. This is because the cross equatorial energy transport adjusts to transport
244 energy away from the warmer hemisphere while the transport of moisture at lower levels in
245 the atmosphere acts in the opposite direction [46,47,48]. This appears to be a general result
246 that is not dependent on the forcing mechanism indicating that it is the inter-hemispheric
247 cooling gradient across the equator rather than the cooling mechanism that determines the
248 model response [12]. Further, the close relationship between cross-equatorial energy transport
249 in the atmosphere and the ITCZ seen in observations [49] is replicated in GCMs [50],
250 providing confidence in the ability to models to reproduce this behaviour. A shift of the ITCZ
251 to the north in any GCM will lead to an increase in the precipitation in the MDR region,
252 which is a well documented proxy for hurricane frequency [13]. Thus, although the detailed
253 impacts may differ compared to those presented here, the general conclusions would likely be
254 similar. Further experiments with other models are, however, the only way to substantiate
255 these assertions.

256 This work reemphasizes the perils of unilateral geoengineering, which might prove attractive
257 to individual actors due to a greater controllability of local climate responses, but with
258 inherent additional risk elsewhere [4,8]. The COP21 target of stabilising global-mean
259 warming at 1.5 K above pre-industrial levels [51] appears extremely difficult to achieve even
260 with measures well beyond what would be considered under conventional mitigation
261 scenarios. The overshoot of 1.5 K could theoretically be combated using SAI (Fig. 3), but if
262 applied just to cool the northern hemisphere, which might have preferential local climate
263 responses (e.g. less Atlantic TCs) for the geoengineering parties, there could be potentially
264 devastating impacts (e.g. Sahelian drought) in other regions. We therefore recommend the
265 expeditious implementation of international regulation to control large-scale SG deployment,
266 in order to develop a truly global approach and deter large-scale unilateral deployment.

267 **2. Methods**

268 **General Circulation Model**

269 HadGEM2-ES is a fully coupled atmosphere–ocean climate model developed by the UK Met
270 Office [52]. The atmospheric sub-model has 38 levels extending to ~40 km, with a horizontal
271 resolution of $1.25^\circ \times 1.875^\circ$ in latitude and longitude, respectively. The model includes the
272 CLASSIC aerosol scheme [53] and an interactive carbon cycle. Briefly, the CLASSIC
273 aerosol scheme was originally designed as a single moment tropospheric scheme where
274 all major aerosol species are treated as separate external mixtures. Of relevance to this
275 study, is the sulphur scheme which oxidises sulfur dioxide to sulfate aerosol via gas
276 phase oxidation by the hydroxyl radical. Aqueous phase oxidation is of little relevance in
277 the stratosphere owing to the low relative humidities and the absence of clouds. Sulphate
278 aerosol is subsequently removed from the stratosphere via dry deposition into the
279 troposphere in the descending branch of the Brewer-Dobson circulation and tropopause
280 folds. The CLASSIC scheme has been shown to adequately represent simulations of e.g.
281 the eruption of Mount Pinatubo in 1991 [32].

282 **HIST, RCP4.5 and Geoengineering simulations**

283 HadGEM2-ES is forced following the Climate Model Intercomparison Project phase 5
284 (CMIP5) protocol using historical data from 1860 to 2005 and RCP4.5 scenarios up to 2100
285 [54]. An ensemble of two HIST and three RCP4.5 simulations are performed. Further detail
286 of the model and simulations is provided in Ref. 11. The G4 scenario follows the GeoMIP

287 protocol [7] and consists of a three member ensemble, while the G4NH and G4SH scenarios
288 use the same total sulphur dioxide (SO_2) injection rate ($5 \text{ Tg}[\text{SO}_2] \text{ y}^{-1}$ from 2020-2070) but
289 concentrated solely in a single hemisphere (north and south, respectively) and are from single
290 simulations. SO_2 is injected evenly between 16 and 25 km altitude (6 model levels) in the
291 geoengineering simulations. Figure 2 shows the resultant SO_4 550nm aerosol optical depth
292 anomalies relative to RCP4.5. It is clear that the geoengineered aerosol is concentrated
293 primarily in the hemisphere of injection, adequately simulating the distribution of aerosol
294 from models with a better resolved stratosphere (Fig. 1). Such hemispherically asymmetric
295 aerosol distributions have been observed subsequent to high latitude volcanic eruptions such
296 as that of Katmai which erupted in Alaska in 1913 [11].

297 **Tracking GCM storms**

298 TC tracking is conducted using the TRACK code (vn. 1.4.7), which has been used for a
299 variety of similar studies [19,55]. For ERA-I we use full Gaussian resolution ($\text{H512} \times \text{256}$)
300 datasets on 6-hour time-steps for JJASON 1979-2014 [28]. The data is firstly spectrally
301 filtered using spherical harmonic decomposition, which translates the HadGEM2-ES and
302 ERA-I data onto a consistent Gaussian grid (128×64 longitudes by latitudes) and truncates
303 wavenumbers less than 5 and greater than 42 (i.e. T42) [55]. Additionally, we employ a
304 Hoskins filter to smooth the data [56]. Vortices are initially identified by TRACK as local
305 maxima in the 850 hPa relative vorticity field that exceeds a threshold of $0.5 \times 10^{-5} \text{ s}^{-1}$ at T42
306 spectral resolution. To identify vortices with a warm core structure (i.e. TCs), we reference
307 the tracks to the vorticity field at the 850, 500, and 250 hPa levels at T63 spectral resolution,
308 using a steepest ascent maximization approach [19]. The criteria used to identify TCs are:-
309 (1) that they attain a lifetime ≥ 2 days (i.e. 8×6 h time steps); (2) that cyclogenesis (defined
310 by first identification) must occur between Equator- 30°N ; (3) that the maximum T63 intensity
311 of relative vorticity at 850 hPa during the lifetime $\geq \zeta_1$ for some chosen value of ζ_1 ; (4) that
312 there must be a T63 vorticity maxima at each level up to 250 hPa and the difference in
313 vorticity between 850 hPa and 250 hPa ($850\text{-}250$) $\geq \zeta_v$ for some chosen value of ζ_v ; (5) that
314 criteria 3 and 4 must be achieved for at least n consecutive 6 h time steps; and finally (6) that
315 they must traverse the North Atlantic hurricane MDR ($[5\text{-}25^\circ\text{N}, 15\text{-}85^\circ\text{W}]$).

316 For HURDAT2 observations [29] we impose the following criteria:- (1) that disturbances
317 must have a lifetime ≥ 2 days, with at least one day within June-November; (2) that the
318 maximum-sustained windspeed exceeds 34 knots; and (3) that they traverse $0\text{-}30^\circ\text{N}$.

319 Previous studies have identified North Atlantic TC frequency and intensity as a key low bias
320 in HadGEM2-ES, which has been attributed to the coarse spatial resolution of the model
321 (~200 km at the equator) [12,23]. However, HadGEM2-ES is able to skilfully capture trends
322 in interdecadal TC frequency when forced by historical conditions if TC-intensity thresholds
323 are relaxed [13,57]. For this investigation, we relax the vorticity thresholds in TRACK when
324 applied to the HadGEM2-ES simulations to obtain reasonable fidelity in annual TC frequency
325 compared with ERA-I and HURDAT2. We test different permutations of $(\zeta_1, \zeta_V, n = 4)$ for
326 ERA-I and HadGEM2-ES against HURDAT2 to obtain reasonable fidelity in annual-mean
327 TCs (Supplementary Note 8). For ERA-I, we find that (6, 5.5, 4) provides the best fit to
328 HURDAT2. For HadGEM2-ES, we find that (4.5, 3.5, 4) provides the best fit to HURDAT2
329 (Fig. 4).

330 **Statistical-dynamical downscaling simulations**

331 The downscaling technique begins by randomly seeding with weak proto-cyclones the large-
332 scale, time-evolving meteorology of the HadGEM2-ES model. These seed disturbances are
333 assumed to move with the reanalysis-provided large-scale flow in which they are embedded,
334 plus a westward and poleward component owing to planetary curvature and rotation. Their
335 intensity is calculated using the Coupled Hurricane Intensity Prediction System (CHIPS, Ref.
336 58), a simple axisymmetric hurricane model coupled to a reduced upper ocean model to
337 account for the effects of upper ocean mixing of cold water to the surface. Applied to the
338 synthetically generated tracks, this model predicts that a large majority of them dissipate
339 owing to unfavorable environments. Only the ‘fittest’ storms survive; thus the technique
340 relies on a kind of natural selection. Extensive comparisons to historical events by Ref. 40
341 and subsequent papers provide confidence that the statistical properties of the simulated
342 events are in line with those of historical tropical cyclones.

343 **Code Availability**

344 The code that supports the findings of this study is available from the corresponding author
345 upon reasonable request. The TRACK model is presently available upon request by emailing
346 K. Hodges (k.i.hodges@reading.ac.uk). The CHIPS model is owned by K. Emanuel
347 (emanuel@mit.edu) to whom service requests should be directed.

348 **Data availability**

349 The data that support the findings of this study are available from the corresponding author
350 upon reasonable request.

351 **References**

352 [1] Crutzen, P., Albedo Enhancement by Stratospheric Sulfur Injections: A Contribution to
353 Resolve a Policy Dilemma?, *Clim. Change*, 77, 3, 211-220, (2006)

354 [2] Shepherd, J. G., *Geoengineering the climate: science, governance and uncertainty*, Royal
355 Society, London, (2009)

356 [3] Irvine, P. J., Kravitz, B., Lawrence, M. G., & Muri, H., An overview of the Earth system
357 science of solar geoengineering, *WIREs Clim Change*, 7, 815–833, (2016)

358 [4] Ricke, K. L., Morgan, M. G., & Allen, M. R., Regional climate response to solar-radiation
359 management, *Nat. Geosci.*, 3(8), 537–541, (2010)

360 [5] Jones, A. C., Haywood, J. M., & Jones, A., Climatic impacts of stratospheric
361 geoengineering with sulfate, black carbon and titania injection, *Atmos. Chem. Phys.*, 16,
362 2843-2862, (2016a)

363 [6] Moore, J. C., *et al.*, Atlantic hurricane surge response to geoengineering, *Proc. Natl.*
364 *Acad. Sci. U. S. A.*, 112(45), 13,794-13,799, (2015)

365 [7] Kravitz, B., *et al.*, The Geoengineering Model Intercomparison Project (GeoMIP). *Atmos.*
366 *Sci. Lett.*, 12: 162–167, (2011)

367 [8] Robock, A., Oman, L., & Stenchikov, G. L., Regional climate responses to
368 geoengineering with tropical and Arctic SO₂ injections, *J. Geophys. Res.*, 113, D16101.,
369 (2008)

370 [9] MacCracken, M. C., On the possible use of geoengineering to moderate specific climate
371 change impacts, *Environ. Res. Lett.*, 4, 045107, doi:10.1088/1748-9326/4/4/045107, (2009)

372 [10] MacMartin, D. G., Keith, D. W., Kravitz, B., & Caldeira, K., Management of trade-
373 offs in geoengineering through optimal choice of non-uniform radiative forcing, *Nat.*
374 *Clim. Change*, 3, 365-368., (2013)

375 [11] Haywood, J. M., Jones, A., Bellouin, N., & Stephenson, D., Asymmetric forcing from
376 stratospheric aerosol impacts Sahelian rainfall, *Nat. Clim. Change*, 3, 660-665, (2013)

- 377 [12] Haywood, J. M., *et al.*, The impact of equilibrating hemispheric albedos on tropical
378 performance in the HadGEM2-ES coupled climate model, *Geophys. Res. Lett.*, 43, 395–403,
379 (2016)
- 380 [13] Dunstone, N. J., Smith, D. M., Booth, B. B. B., Hermanson, L., & Eade, R.,
381 Anthropogenic aerosol forcing of Atlantic tropical storms, *Nature Geosci.*, 6, 534–539,
382 (2013)
- 383 [14] Merlis, T. M., Zhao, M., & Held, I. M., The sensitivity of hurricane frequency to ITCZ
384 changes and radiatively forced warming in aquaplanet simulations, *Geophys. Res. Lett.*, 40,
385 4109–4114, (2013)
- 386 [15] Goldenberg, S. B., Landsea, C. W., Mestas-Nunez, A. M., & Gray, W. M., The recent
387 increase in Atlantic hurricane activity: Causes and implications, *Science*, 293 (5529), 474–
388 479, (2001)
- 389 [16] Evan, A. T., Atlantic hurricane activity following two major volcanic eruptions, *J.*
390 *Geophys. Res.*, 117, D06101, (2012)
- 391 [17] Guevara-Murua, A., Hendy, E. J., Rust, A. C., & Cashman, K. V., Consistent decrease in
392 North Atlantic Tropical Cyclone frequency following major volcanic eruptions in the last
393 three centuries, *Geophys. Res. Lett.*, 42, 9425–9432, (2015)
- 394 [18] Jones, C. D., *et al.*, The HadGEM2-ES implementation of CMIP5 centennial
395 simulations, *Geosci. Model Dev.*, 4(3), 543–570, (2011)
- 396 [19] Bengtsson, L., Hodges, K. I., & Esch, M., Tropical cyclones in a T159 resolution global
397 climate model: comparison with observations and re-analyses, *Tellus A*, 59 (4), 396-416,
398 (2007)
- 399 [20] Latif, M., Keenlyside, N., & Bader, J., Tropical sea surface temperature, vertical wind
400 shear, and hurricane development, *Geophys. Res. Lett.*, 34, L01710, (2007)
- 401 [21] Villarini, G., and Vecchi, G. A., Twenty-first-century projections of North Atlantic
402 tropical storms from CMIP5 models. *Nature Clim. Change*, 2, 604–607, (2012)
- 403 [22] Emanuel, K., Ravela, S., Vivant, E., & Risi, C., A statistical deterministic approach to
404 hurricane risk assessment, *Bull. Am. Meteorol. Soc.*, 87, 299–314, (2006)

- 405 [23] Camargo, S. J., Global and regional aspects of tropical cyclone activity in the CMIP5
406 models. *J. Clim.*, 26, 9880–9902, (2013)
- 407 [24] Emanuel, K. A., Downscaling CMIP5 climate models shows increased tropical cyclone
408 activity over the 21st century, *Proc. Natl. Acad. Sci.*, 110(30), 12,219–12,224, (2013)
- 409 [25] Knutson, T. R., *et al.*, Tropical cyclones and climate change, *Nat. Geosci.*, 3, 157–163,
410 (2010)
- 411 [26] Knutson, T. R., *et al.*, Global projections of intense tropical cyclone activity for the late
412 21st century from dynamical downscaling of CMIP5/RCP4.5 scenarios, *J. Clim.*, 28(18),
413 7203–7224, (2015)
- 414 [27] Camargo, S. J. and Zebiak, S. E., Improving the detection and tracking of tropical storms
415 in atmospheric general circulation models. *Wea. Forecasting* 17, 1152–1162, (2002)
- 416 [28] Dee, D. P., *et al.*, The ERA-Interim reanalysis: configuration and performance of the data
417 assimilation system. *Q.J.R. Meteorol. Soc.*, 137: 553–597., (2011)
- 418 [29] Landsea, C. W., & J. L. Franklin, Atlantic hurricane database uncertainty and
419 presentation of a new database format, *Mon. Weather Rev.*, 141, 3576–3592., (2013)
- 420 [30] Oman, L., Robock, A., Stenchikov, G. L., & Thordarson, T., High-latitude eruptions cast
421 shadow over the African monsoon and the flow of the Nile. *Geophys. Res. Lett.* 33, L18711,
422 (2006)
- 423 [31] English, J. M., Toon, O. B., & Mills, M., Microphysical simulations of large volcanic
424 eruptions: Pinatubo and Toba, *J. Geophys. Res. Atmos.*, 118, 1880–1895, (2013)
- 425 [32] Jones, A. C., Haywood, J. M., Jones, A., & Aquila, V., Sensitivity of volcanic aerosol
426 dispersion to meteorological conditions: A Pinatubo case study, *J. Geophys. Res. Atmos.*,
427 121, 6892–6908, (2016b)
- 428 [33] Davidson, P., Burgoyne, C. Hunt, H., & Causier, M., Lifting options for stratospheric
429 aerosol geoengineering: advantages of tethered balloon system, *Phil. Trans. R. Soc. A*, 370,
430 4263–4300, (2012)

- 431 [34] Timmreck, C., Graf, H.-F., & Kirchner, I., A one and half year interactive
432 MA/ECHAM4 simulation of Mount Pinatubo Aerosol, *J. Geophys. Res.*, 104(D8), 9337–
433 9359, (1999)
- 434 [35] Weisenstein, D. K., Penner, J. E., Herzog, M., & Liu, X., Global 2-D intercomparison of
435 sectional and modal aerosol modules, *Atmos. Chem. Phys.*, 7, 2339–2355, (2007)
- 436 [36] Dhomse, S. S., *et al.*, Aerosol microphysics simulations of the Mt. Pinatubo eruption
437 with the UM-UKCA composition-climate model, *Atmos. Chem. Phys.*, 14, 11,221–11,246,
438 (2014)
- 439 [37] Jones, A., *et al.*, The impact of abrupt suspension of solar radiation management
440 (termination effect) in experiment G2 of the Geoengineering Model Intercomparison Project
441 (GeoMIP), *J. Geophys. Res. Atmos.*, 118, 9743–9752, (2013)
- 442 [38] Compo, G. L. *et al.*, The twentieth century reanalysis project. *Quart. J. R. Meteorol. Soc.*
443 137, 1–28, (2011)
- 444 [39] Rayner, N. A., Parker, D. E., Horton, E. B., Folland, C. K., Alexander, L. V., Rowell, D.
445 P., Kent, E. C., & Kaplan, A., Global analyses of sea surface temperature, sea ice, and night
446 marine air temperature since the late nineteenth century. *J. Geophys. Res.*, 108, 4407, (2003)
- 447 [40] Emanuel, K., Sundararajan, R., & Williams, J., Hurricanes and global warming: Results
448 from downscaling IPCC AR4 simulations. *Bull. Amer. Meteor. Soc.*, 89, 347-367, (2008)
- 449 [41] Grinsted A, Moore, J. C., & Jevrejeva, S., Projected Atlantic tropical cyclone threat from
450 rising temperatures, *Proc. Natl. Acad. Sci.*, 110(14):5369–5373, (2013)
- 451 [42] Murakami, H., Hsu, P.-C., Arakawa, O., & Li., T., Influences of model biases on
452 projected future changes in tropical cyclone frequency of occurrence. *J. Clim.*, 27, 2159–
453 2181, (2014)
- 454 [43] Walsh, K. J. E., *et al.*, Hurricanes and climate: The U.S. CLIVAR working group on
455 hurricanes, *Bull. Am. Meteorol. Soc.*, 96(6), 997–1017, (2015)
- 456 [44] Landsea, C. W., & Gray, W. M., The strong association between western sahelian
457 monsoon rainfall and intense Atlantic hurricanes. *J. Clim.*, 5, 435–453., (1992)

- 458 [45] Kravitz, B, Robock, A., Forster, P. M., Haywood, J. M., Lawrence, M. G., & Schmidt,
459 H., An overview of the Geoengineering Model Intercomparison Project (GeoMIP), *J.*
460 *Geophys.Res.Atmos.*, 118, 13,103–13,107, (2013)
- 461 [46] Hwang, Y. T., & Frierson, D. M., Link between the double-intertropical convergence
462 zone problem and cloud biases over the Southern Ocean, *Proc. Natl. Acad. Sci.*, 110(13),
463 4935–4940, (2013)
- 464 [47] Stephens G. L, Hakuba, M. Z., Hawcroft, M., Haywood, J. M., Behrangi, A., Kay, J. E.,
465 & Webster, P. J., The curious nature of the hemispheric symmetry of the Earth's water and
466 energy balances. *Curr. Clim. Chang. Rep.* , 2(4):135–147, (2016)
- 467 [48] Hawcroft, M., Haywood, J. M., Collins, M., Jones, A., Jones, A. C., & Stephens, G.,
468 Southern Ocean albedo, inter-hemispheric energy transports and the double ITCZ: Global
469 impacts of biases in a coupled model, *Clim. Dyn.*, 48, 7–8, 2279–2295, (2016)
- 470 [49] Schneider T., Bischoff, T., & Haug, G. H., Migrations and dynamics of the intertropical
471 convergence zone. *Nature*, 513(7516):45–53, (2014)
- 472 [50] Loeb N. G., Wang, H., Cheng, A., Kato, S., Fasullo, J. T., Xu, K.-M., & Allan, R.,
473 Observational constraints on atmospheric and oceanic cross-equatorial heat transports:
474 revisiting the precipitation asymmetry problem in climate models. *Clim. Dyn.* 46, 9-10,
475 3239–3257, (2015)
- 476 [51] UNFCCC, Adoption of the Paris Agreement FCCC/CP/2015/L.9/Rev.1, (2015)
- 477 [52] Collins, W. J., *et al.*, Development and evaluation of an Earth-system model -
478 HadGEM2, *Geosci. Model Dev.*, 4, 1051–1075, (2011)
- 479 [53] Bellouin, N., Rae, J., Jones, A., Johnson, C., Haywood, J., & Boucher, O., Aerosol
480 forcing in the CMIP5 simulations by HadGEM2-ES and the role of ammonium nitrate, *J.*
481 *Geophys. Res.*, 116, D20206, (2011)
- 482 [54] Taylor, K. E., Stouffer, R. J., & Meehl, G. A., An overview of CMIP5 and the
483 experiment design, *Bull. Am. Meteorol. Soc.*, 93(4), 485–498, (2012)
- 484 [55] Hoskins, B. J., & Hodges, K. I., New perspectives on the Northern Hemisphere winter
485 storm tracks, *J. Atmos. Sci.*, 59, 1041–1061, (2002)

486 [56] Sardeshmukh, P. D., & Hoskins, B. J., Spectral smoothing on the sphere, *Mon. Wea.*
487 *Rev.*, 112, 2524–2529, (1984)

488 [57] Smith, D. M., Eade, R., Dunstone, N. J., Fereday, D., Murphy, J. M., Pohlmann, H., &
489 Scaife, A. A., Skilful multi-year predictions of Atlantic hurricane frequency, *Nat. Geosci.*, 3,
490 846–849, (2010)

491 [58] Emanuel, K., DesAutels, C., Holloway, C., & Korty, R., Environmental control of
492 tropical cyclone intensity. *J. Atmos. Sci.*, 61, 843-858, (2004)

493 **End Notes**

494 **Acknowledgments**

495 A.C.J. was supported by a Met Office/NERC CASE (ref. 580009183) PhD studentship.
496 M.K.H. and J.M.H. were supported by the Natural Environment Research
497 Council/Department for International Development via the Future Climates for Africa
498 (FCFA) funded project ‘Improving Model Processes for African Climate’ (IMPALA,
499 NE/M017265/1).

500 **Competing interests**

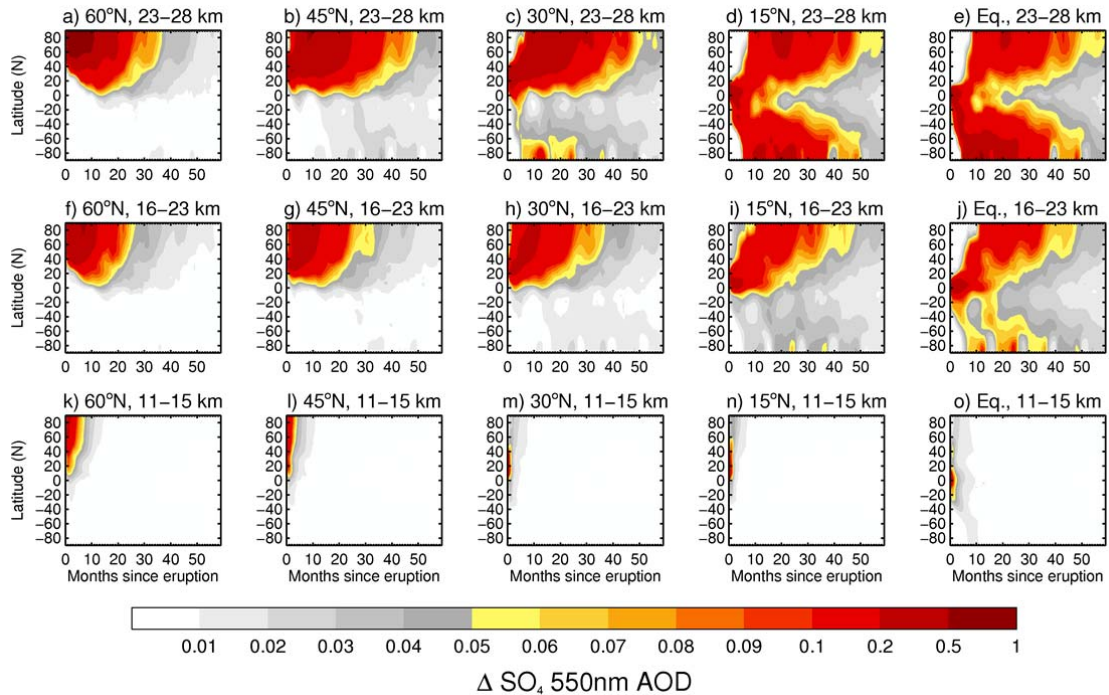
501 The authors declare no competing financial interests.

502 **Author Contributions**

503 A.C.J. performed the analysis with assistance from J.M.H, K.I.H. and M.H., and wrote the
504 paper with assistance from all co-authors. J.M.H., A.J. and N.D. designed the study and A.J.
505 conducted the simulations. K.E. conducted the statistical downscaling simulations and
506 assisted in the analysis.

507

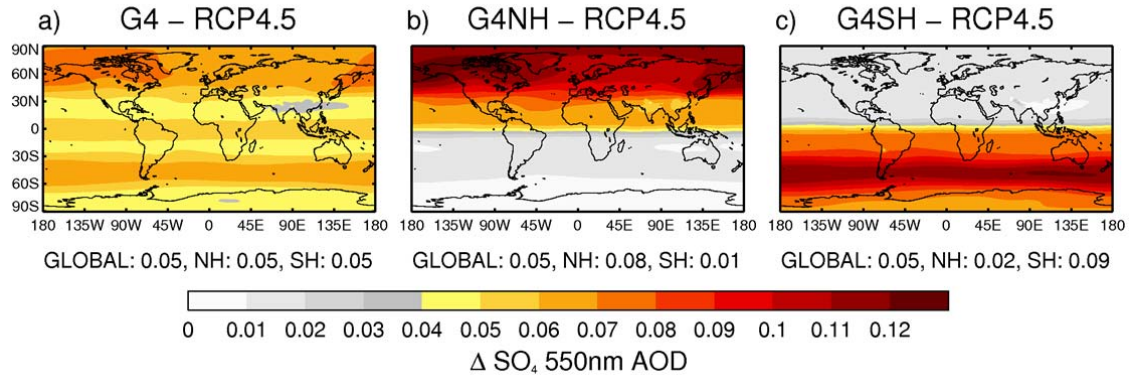
508



509

510 **Figure 1 | Investigating the sensitivity of aerosol dispersion to the altitude and latitude**
 511 **of a volcanic eruption.** 5 y evolution of the anomaly in sulfate (SO_4) aerosol optical depth
 512 (AOD) for injections of sulfur dioxide into the Northern Hemisphere. Latitudes progress from
 513 60°N in the left column (**a, f, k**) to the Equator in the right column (**e, j, o**) and injection
 514 altitudes from 23-28 km in the top row (**a-e**) to 11-15 km in the bottom row (**k-o**).
 515 Simulations are with a ‘high-top’ version of the HadGEM2 model with stratospheric layers
 516 up to 80 km using the CLASSIC aerosol scheme [32].

517

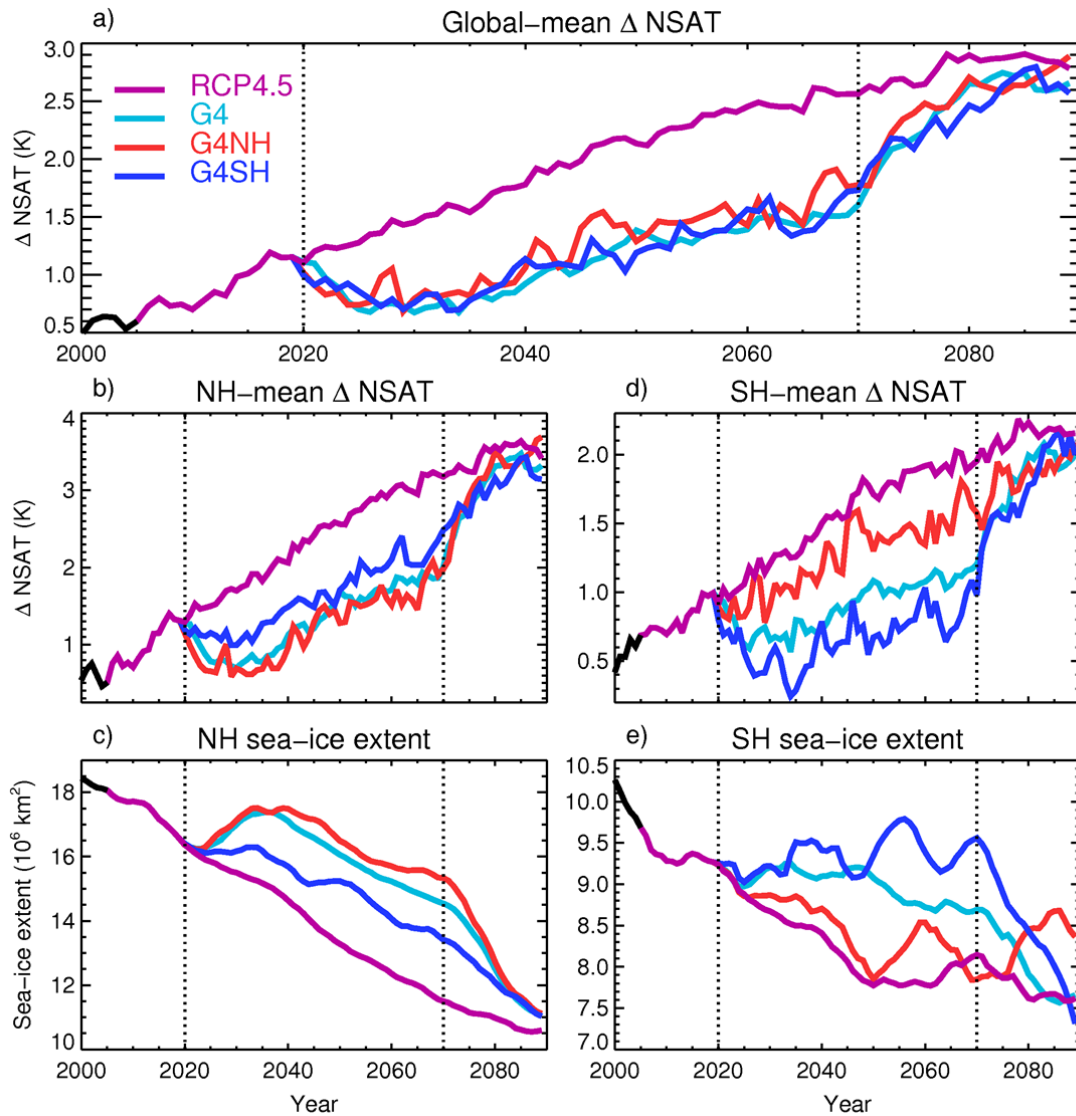


518

519 **Figure 2 | Aerosol optical depth anomalies in the solar geoengineering simulations.**
 520 Sulfate (SO_4) 550nm aerosol optical depth (AOD) anomaly 2020-2070 for **a**, global solar
 521 geoengineering (G4); **b**, northern hemisphere solar geoengineering (G4NH); and **c**, southern
 522 hemisphere solar geoengineering (G4SH) relative to RCP4.5

523

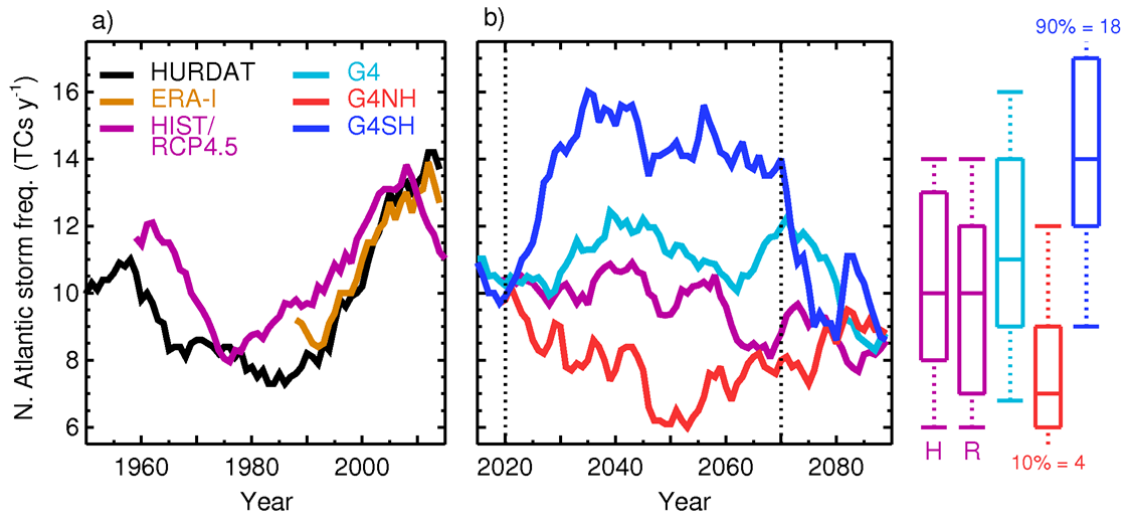
524



525

526 **Figure 3 | 21st Century temperature and sea-ice changes.** **a**, Global-mean near-surface air
 527 temperature (NSAT) anomaly relative to a 240 y pre-industrial control simulation for
 528 RCP4.5, global solar geoengineering (G4), northern hemisphere (NH) solar geoengineering
 529 (G4NH), and southern hemisphere (SH) solar geoengineering G4SH; **b-c**, NH NSAT
 530 anomaly and total sea-ice extent (10^6 km²); **d-e**, SH NSAT anomaly and total sea-ice extent.
 531 Sea-ice extents are smoothed by a 10 y simple moving average. Vertical dotted lines at years
 532 2020 and 2070 indicate the start and cessation of solar geoengineering respectively.

533

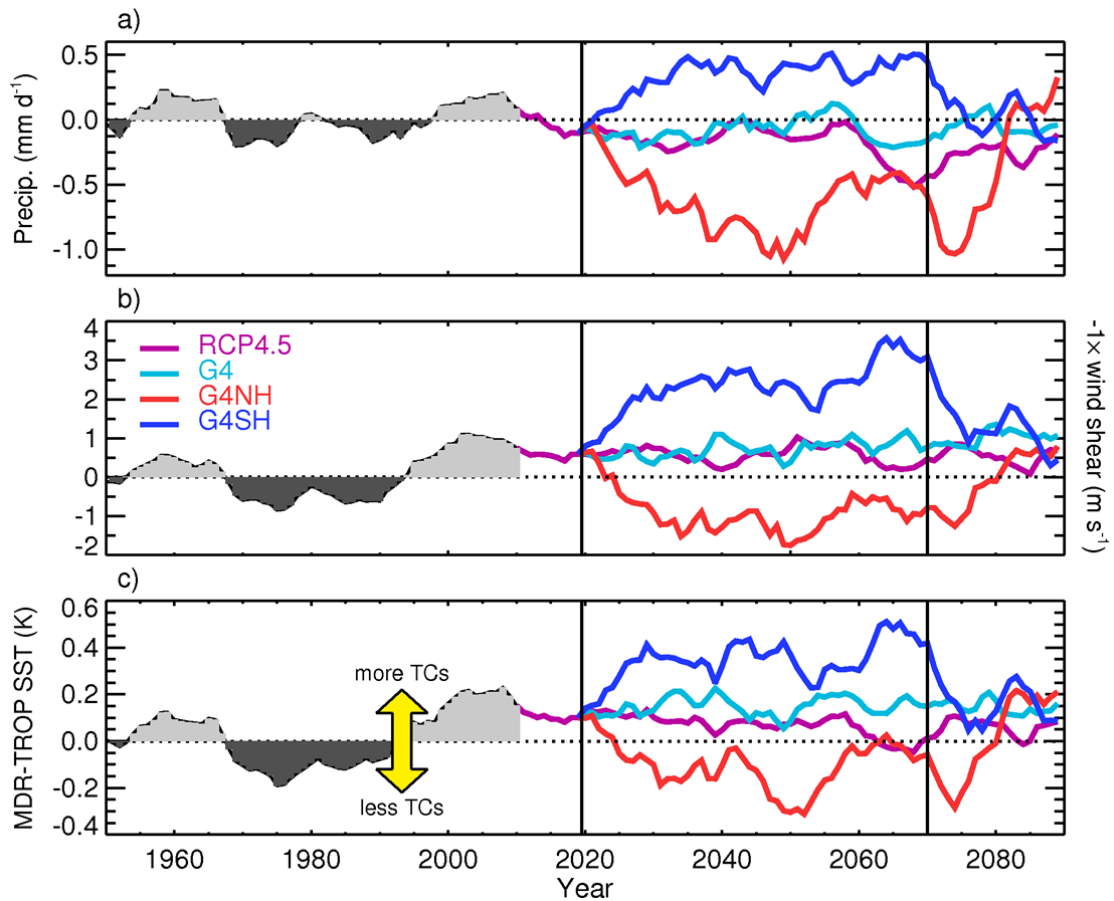


534

535

Figure 4 | Observed and simulated Tropical Cyclone frequency. **a**, Historical tropical cyclone (TC) frequencies, smoothed by a 10 y simple moving average, for ERA-I [28], the ensemble mean of the HadGEM2-ES HIST simulations and HURDAT2 observations [29]. **b**, the same as **a** but for the RCP4.5 and SAI simulations. The box and whisker plots (right) show the 10, 25, 50, 75, and 90% quantiles of the HIST ('H', 1950-2000), RCP4.5 ('R', 2020-2070) and SAI (2020-2070) raw annual TC frequency. G4 refers to a global SAI scenario, G4NH refers to a northern hemisphere SAI scenario, and G4SH refers to a southern hemisphere SAI scenario. Vertical dotted lines at years 2020 and 2070 (**b**) indicate the start and cessation of solar geoengineering respectively.

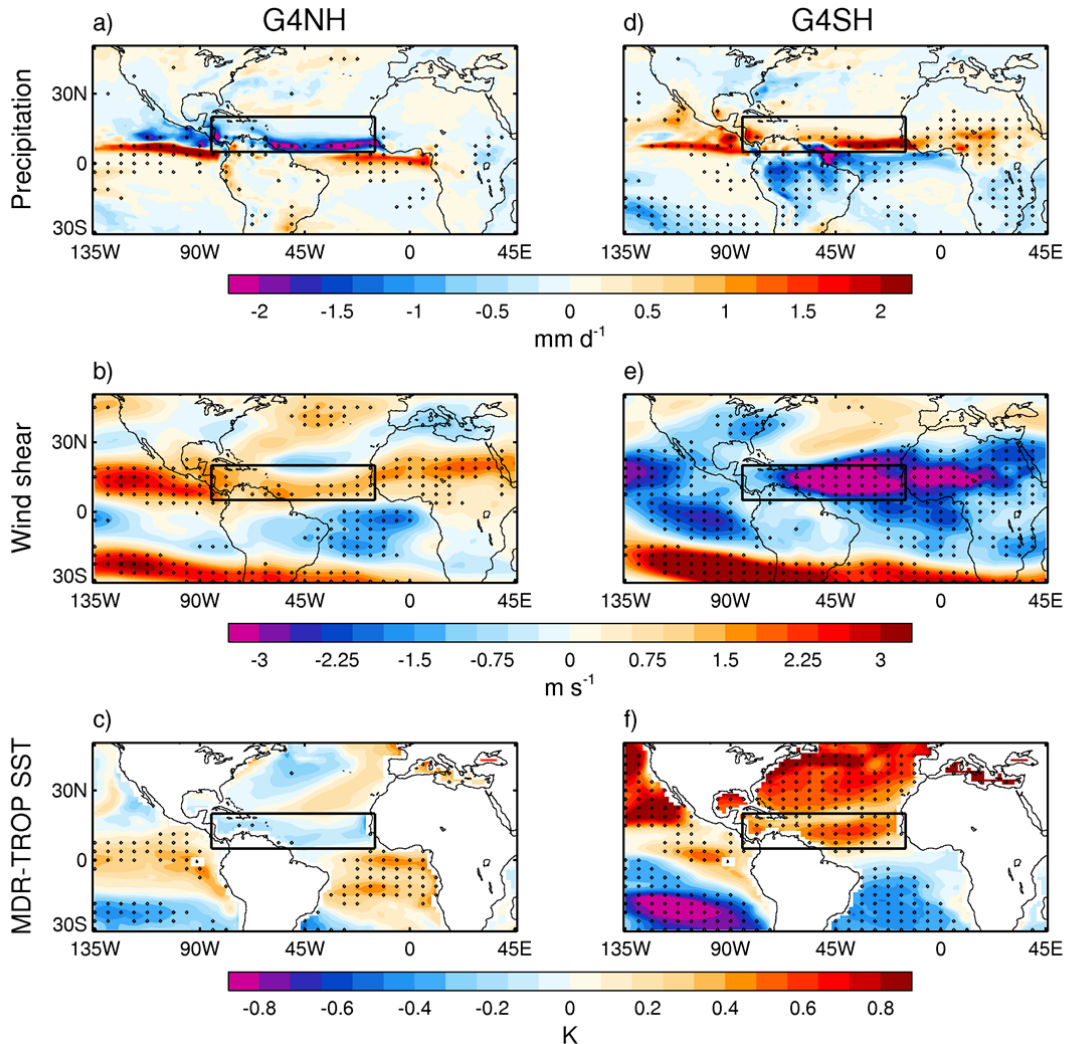
543



544

545 **Figure 5 | Modelled Tropical Cyclone-related climate indices.** **a**, June-November
 546 (JJASON) precipitation anomaly (relative to 1950-2000) averaged over the hurricane main
 547 development region (MDR) [5-°20N, 15-85°W]. **b**, the same as **a** but for inverse vertical
 548 zonal-wind shear. **c**, the same as **a** but for relative SST. G4 refers to a global SAI scenario,
 549 G4NH refers to a northern hemisphere SAI scenario, and G4SH refers to a southern
 550 hemisphere SAI scenario. Vertical lines at years 2020 and 2070 indicate the start and
 551 cessation of solar geoengineering respectively.

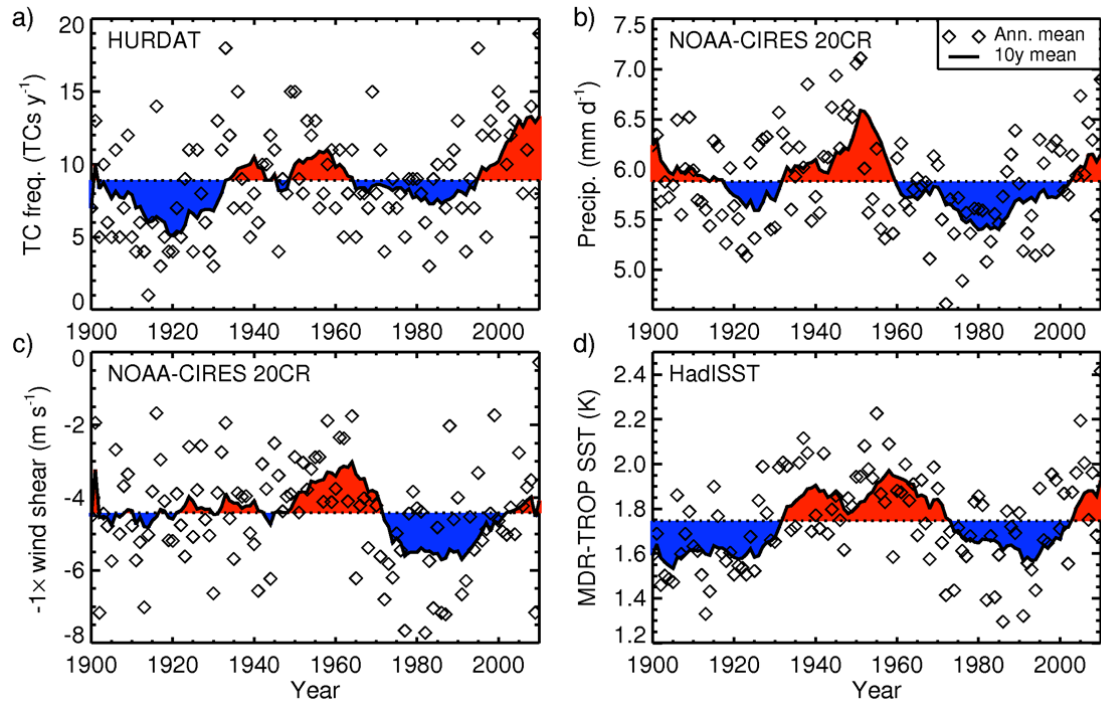
552



554

555 **Figure 6 | Climate anomalies in the hemispheric solar geoengineering simulations. a,**
 556 Northern hemisphere only solar geoengineering (G4NH) 2020-2070 JJASON precipitation
 557 anomaly relative to 1950-2000. **b,** the same as **a** but for vertical zonal-wind shear. **c,** the same
 558 as **a** but for relative SST. **d-f,** the same as **a-c** but for southern hemisphere only solar
 559 geoengineering (G4SH). Stippled regions on the maps show where differences are outside the
 560 90% variability of a 240 y pre-industrial control ensemble mean. The hurricane main
 561 development region (MDR, [5-20°N, 15-85°W]) is marked by black rectangles.

562



563

564 **Figure 7 | 20th Century North Atlantic climate indices from observations and reanalyses.**

565 June-November (JJASON) observations and reanalysis data time series for: **a**, TC frequency

566 [29]; **b**, hurricane main development region (MDR, [5-20°N, 15-85°W]) precipitation and **c**,

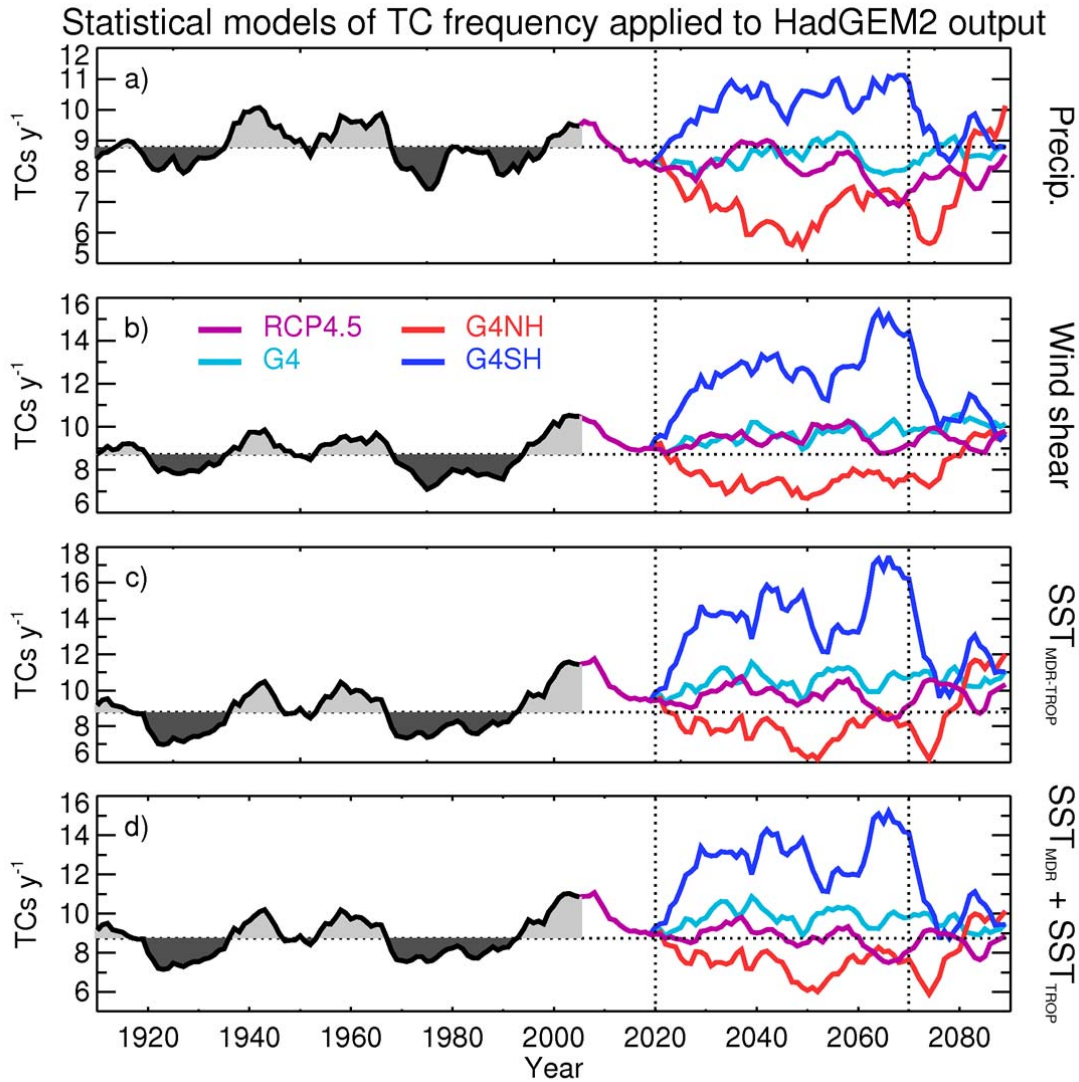
567 wind shear [38]; and **d**, sea-surface temperature (MDR minus the Tropics) [39]. Diamonds

568 indicate JJASON average quantities for each year in the MDR or North Atlantic basin, and

569 thick black lines denote 10 y moving averages. Red (blue) regions indicate where moving

570 averages are above (below) the 1900-2010 mean values

571



572

573 **Figure 8 | Tropical Cyclone frequency inferred from various statistical relationships**

574 **with climate indices.** TC frequency inferred from HadGEM2-ES meteorology using

575 statistical relationships developed from historical observations and reanalyses. The covariates

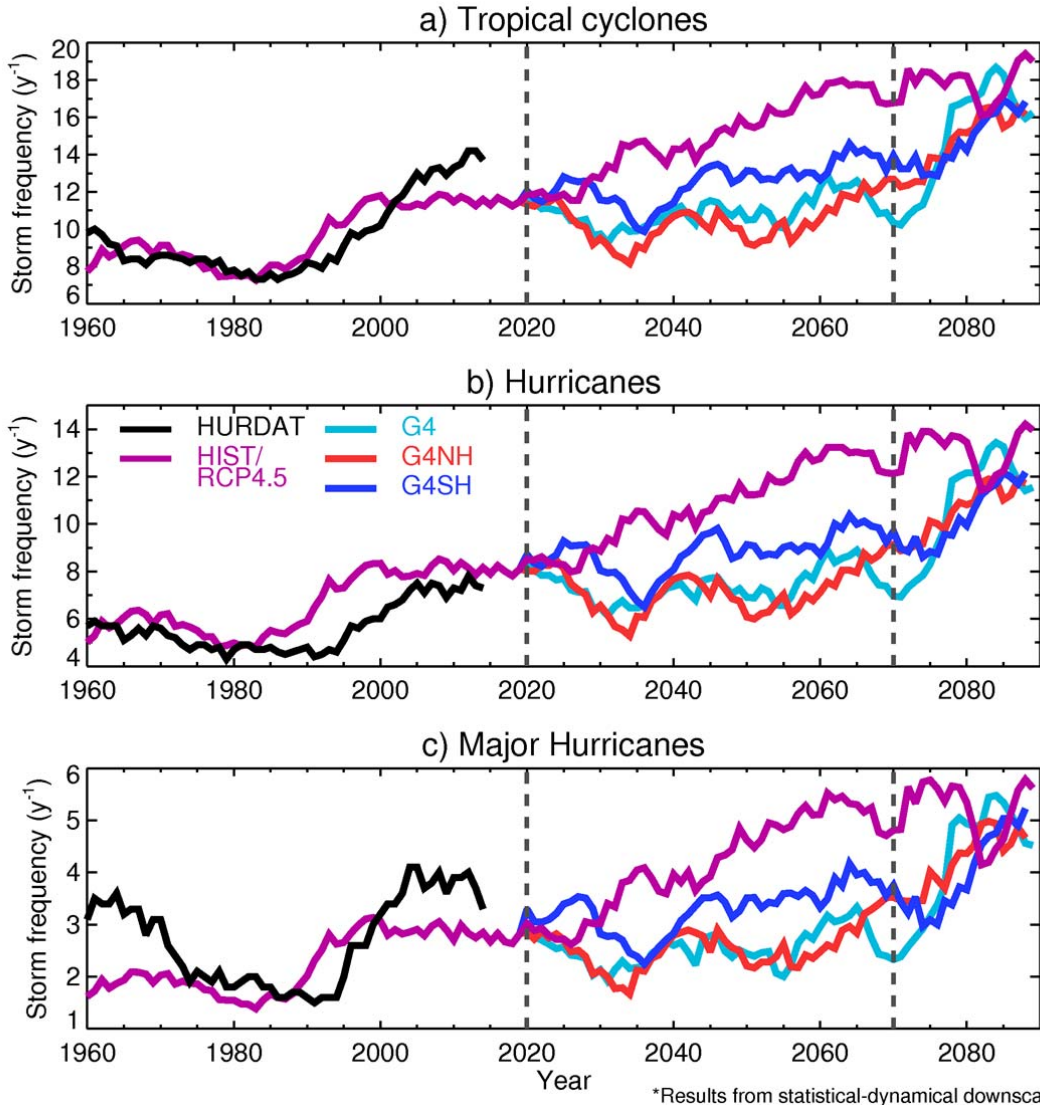
576 used are: **a**, MDR precipitation; **b**, MDR wind shear; **c**, relative sea-surface temperatures

577 (MDR minus tropical mean); and **d**, MDR and tropical SSTs as separate covariates. Vertical

578 dotted lines at years 2020 and 2070 indicate the start and cessation of solar geoengineering

579 respectively.

580



581

582 **Figure 9 | Tropical Cyclone frequency from downscaling simulations. a,** North Atlantic
 583 tropical cyclone (max windspeed $> 20 \text{ m s}^{-1}$) frequency from downscaling simulations using
 584 HadGEM2-ES simulated meteorology plotted with observed (HURDAT) TC frequencies. All
 585 smoothed with 10 y simple moving averages. **b,** the same as **a** but for hurricane (max
 586 windspeed $> 37 \text{ m s}^{-1}$) frequency. **c,** the same as **a** and **b** but for major hurricane (max
 587 windspeed $> 96 \text{ m s}^{-1}$) frequency. G4 refers to a global SAI scenario, G4NH refers to a
 588 northern hemisphere SAI scenario, and G4SH refers to a southern hemisphere SAI scenario
 589 Vertical dashed lines at years 2020 and 2070 indicate the start and cessation of solar
 590 geoengineering respectively.